ISCI, Volume *20*

Supplemental Information

Difference between Metal-S and Metal-O Bond Orders: A Descriptor of Oxygen Evolution Activity for Isolated Metal Atom-Doped MoS_2 Nanosheets

Guangtong Hai, Hongyi Gao, Guixia Zhao, Wenjun Dong, Xiubing Huang, Yi Li, and Ge Wang

iScience

Supplemental Information

Difference between Metal-S and Metal-O bond order: A descriptor of oxygen evolution performance for isolated metal atom-doped MoS_2 nanosheets

Guangtong Hai, Hongyi Gao, Guixia Zhao, Wenjun Dong, Xiubing Huang, Yi Li, and Ge Wang

Transparent Methods

Theoretical calculations

All the spin-polarized calculations were based on the density functional theory (DFT) with the combination of atomic orbitals (LCAO) method. The general gradient approximation (GGA) was used throughout with the revised Perdew-Burke-Ernzerhof (RPBE) parametrized exchange-correlation functional. Besides, a polarized basis set of double numerical plus polarization was employed to expand the wavefunction with a fine integration grid during the calculations. To obtain an accurate result, a large orbital cutoff of 6.5 Å was applied, and the relativistic effect of heavy metal atoms was treated using DFT semi-core pseudopots core treatment method to describe the electron-ion interaction.

All the model structures were built with Mo-top binding configuration on plane (002). The desired surface was modeled with two MoS_2 layers, which is consistent with the atomic force microscope (AFM) results. A sufficient large vacuum slab of 15 Å was used to eliminate the interactions between MoS_2 layers and the dipole correction was applied along the surface normal vector.

During the geometry optimizations, all the atoms were relaxed and optimized to the ground state with no imaginary frequency. To obtain the energy of the ground state exactly, the magnetic state of transition metal atoms including high and low spin state were considered, and the lowest energy structure was used as the ground state. Specially, the basis set superposition error (BSSE) correction was applied for a credible adsorption energy with M-UMONs specified to Counterpoise1 and adsorbed *OH specified to Counterpoise 2. To improve the computational efficiency, the delocalized internal coordinate was applied. Here, the surface cell was extended to a (4 × 4 × 1) supercell due to the mass loading of single atoms is usually below 10 %, and this model was basically consistent to subsequent atomic percentage results derived from the ICP-MS results shown in Table. S2. The (5 × 5 × 1) k-point grid was used for Brillouin-zone integrations. The O_2 and H_2O molecules

were optimized in a (10 × 10 × 10) $Å^3$ box with a Gamma point only k-point set. The convergence criteria was 10^{-7} for self-consistent field calculations, the model structures were optimized until the max force is below 0.003 Ha/Å and energy change is below 10^{-5} Hartree. Furthermore, the conductor-like screening model was used to describe the solvation effects, and the dielectric constant of solvent (water) was set to 78.54.

According to the frontier orbitals and electrostatic potential (ESP) calculations, we proposed that the surface transitional metal sites are the main active sites, so the reaction mechanism calculations were based on these metal sites. A fine grid with the interval of 0.15 Å was applied in the ESP calculations. The k-point set is (5 × 5 × 1) for the ESP calculations and Gamma point only for orbitals calculations.

The thermodynamic properties were obtained from the frequency calculations. Besides, the bond population calculations were employed to obtain the M-S and M-O bond orders information. Because the Milliken bond orders are strongly depended on the choice of basis set, more transferable Mayer bond orders are applied here, which is suitable for describing similar molecules (Mayer, 1986). The definition of Mayer bond order was shown below:

$$B_{\mathrm{AB}} = 2\sum_{\mu\in A}\sum_{v\in B}[(P^{\alpha}S)_{\mu v}(P^{\alpha}S)_{v\mu} + \left(P^{\beta}S\right)_{\mu v}\left(P^{\beta}S\right)_{v\mu}]$$

Here, B_{AB} is the bond orders between atom A and atom B. P^{α}, P^{β} are the density matrices for spin α and β. According to our test results shown below, when the basis set was changed, the Mayer bond orders was almost unchanged, which is transferable for different basis sets.

In Mo-top binding configuration model structure, each surface transitional metal atom is coordinated with three S atoms (MS_3 coordinate units), and these three M-S bond order values are unequal, so the averaged value is applied to estimate the bond orders. According to our test, the M-S and M-O bond orders values in different OER steps are also variable, but the differences are very small, so the same values in adsorption

configurations of step 1 were applied for simplicity, that is, the M-S and M-O bond orders were all derived from the "HO-M-MoS_2" configuration in step 1.

As for the theoretical overpotential (denoted as η) calculations, four-electron sequent transport mechanism was applied. As shown below, the Gibbs free energy change for four steps was denoted as G_1, G_2, G_3, G_4 and G_5, respectively.

1. M-MoS_2 + OH^- → HO-M-MoS_2 + e^- $\Delta G = G_1$

2. HO-M-MoS_2 + OH^- → O-M-MoS_2 + H_2O + e^- $\Delta G = G_2$

3. O-M-MoS_2 + OH^- → HOO-M-MoS_2 + e^- $\Delta G = G_3$

4. HOO-M-MoS_2 + OH^- → OO-M-MoS_2 + H_2O + e^- $\Delta G = G_4$

5. OO-M-MoS_2 → M-MoS_2 + O_2 $\Delta G = G_5$

The Gibbs free energy change could be transformed to the potential through the formula below:

$$E \text{ (vs. SHE)} = - (-\Delta G - \Delta G^{SHE}) / nF$$

Here, ΔG is the Gibbs free energy change, and the maximum ΔG value of G_1, G_2, G_3, G_4 and G_5 should be used to calculate the theoretical overpotential, n is the number of moles of electrons in the reaction, F is Faraday constant (96485 C mol^{-1}), respectively. Since the OER is an oxidation reaction, the $-\Delta G$ values (the Gibbs free energy of corresponding reduction reaction) were applied to calculate the standard electrode potential. ΔG^{SHE} is the Gibbs free energy change of the reduction of the proton ($H^+ + e^- \rightarrow 1/2\ H_2$), and we adopt the experimental value, ΔG^{SHE} = -418 kJ/mol (Torres et al., 2011).

According to the Nernst equation, the potential of work electrode (vs. SHE) could be transformed to the potential versus reversible hydrogen electrode (RHE) by the formula: E (vs. RHE) = E (vs. SHE) + 0.0592 pH. The thermodynamic potential of OER (E_0 H_2O/O_2 = 1.23 V vs. RHE) is used as reference to obtain the theoretical

overpotential through the formula: $\eta = E$ (vs. RHE) – 1.23 = E (vs. SHE) + 0.0592 pH - 1.23. In this work, the theoretical overpotential calculations were based on the conditions of pH = 14 (alkaline condition).

In this work, all the possible descriptors were taken into consideration in data analysis. For easily production run, we were aimed to obtain a convenient linear correlation between the descriptor and the overpotential. Hence, all the data correlation analysis were based on the linear regression (LR) algorithms. Candidate descriptors that without linear correlation with overpotential were all ruled out to be applied as the final desired descriptor. After the analysis and screening, the difference between M-S and M-O bond orders were found to most strongly correlated with overpotential and then reasonably to be employeed as the descriptor.

Preparation of different M-UMONs

1 mmol of hexaammonium heptamolybdate tetrahydrate (HHT) and 30 mmol of thiourea were dissolved in 35 mL water with vigorous stirring to obtain the uniform solution and then transferred to a 50 mL reaction kettle and maintained at 493 K for 20 h. Then the product was washed with water for three times and frozen drying. The obtained MoS_2 nanosheets were stored in an air tight test tube.

To obtain different kinds of M-UMONs, 0.05 mmol of associated transition metal salt, that is, nickel acetate tetrahydrate for Ni-UMONs, cobalt acetate tetrahydrate for Co-UMONs, copper acetate for Cu-UMONs, zinc acetate dihydrate for Zn-UMONs, manganese acetate tetrahydrate for Mn-UMONs, palladium acetate for Pd-UMONs, ferric(II) acetate tetrahydrate for Fe-UMONs, chloroauric acid for Au-UMONs, chloroplatinic acid hexahydrate for Pt-UMONs, vanadium dichloride for V-UMONs, chromium acetate for Cr-UMONs; and 18 mg of thiourea were added to 2 mL of mixed solution of water and ethanol, and then left overnight. Subsequently this mixed solution was added into 50 mL of 1 mg mL^{-1} MoS_2 colloid (12 mL of isopropanol, 38 mL of water with 50 mg of polyvinylpyrrolidone (PVP)) with vigorous stirring for 30 min. The colloid was then transferred to a 100 mL reaction kettle, and maintained at 433 K for 24 h. After the hydrothermal treatment, the product was washed

three times using water and then frozen dried under vacuum for 6 h. To avoid the aggregation and self-nucleation of these transition metal atoms, very low concentration of associated transition metal saline solution was used in this work (Liu et al., 2017). Therefore, we repeated above procedures three times to achieve a desired mole number loading.

Electrochemical measurements

The electrochemical measurements were carried out through a Princeton PMC 1000 & 500 electrochemical workstation with a typical three-electrode configuration. The as-prepared M-UMONs were dispersed in a mixed solution of 0.5 mL ethanol, 0.03 mL 5 wt % Nafion solution. After ultrasonication for 30 min, the mixed solution was dropped on the glass-carbon electrode (GCE) uniformly, and then used as the working electrode. Here, we assumed that the OER activity was mainly from the supported transition metal atoms, based on this, the moles numbers of loaded transition metal atoms were all kept at 2.0 μmol for different kinds of M-UMONs to make the results comparable. The saturate calomel electrode was applied as reference electrode and a small platinum foil (1 cm × 1 cm) worked as the counter electrode, respectively. To obtain a credible result, the LSV curves were recorded at a low scan rate of 5 mV s^{-1}, which is able to minimize the capacitive current (Stevens et al., 2017; Zhuang et al., 2014). The chronoamperometric test was performed at the overpotential of 0.25 V. In this work, we normalized the specific activity by the amount of active metal atoms. To make the comparison meaningful, the moles numbers of Ru atoms were also kept at 2.0 μmol, that is 2 μmol of RuO_2 (0.26 mg RuO_2) during the electrochemical measurements of RuO_2. In addition, all the potentials were calibrated to RHE by the formula: $E_{RHE} = E_{SCE} + 0.24 + 0.0592$ pH. The electrolyte used in this work was 1 M KOH (high-purity) solution and the impedance of 1 M KOH solution at ambient temperature was measured at about 9 Ω, and all the data were corrected with iR-compensation.

Characterizations

The high-angle annular dark field scanning transmission electron microscope (HAADF-STEM) image was recorded by an aberration-corrected transmission electron microscopy (Cs-corrected TEM) (FEI Titan 80-300). The TEM images were recorded by a field emission high resolution transmission electron microscopy (JEOL JEM-2010). The thickness of these sample was measured by an AFM (Shimadzu SPM-960). The crystal structures were defined by XRD (Bruke D8 Advance diffractometer, Cu Kα1). The ICP-MS was measured by the Agilent 7500ce system.

Supplemental Figures

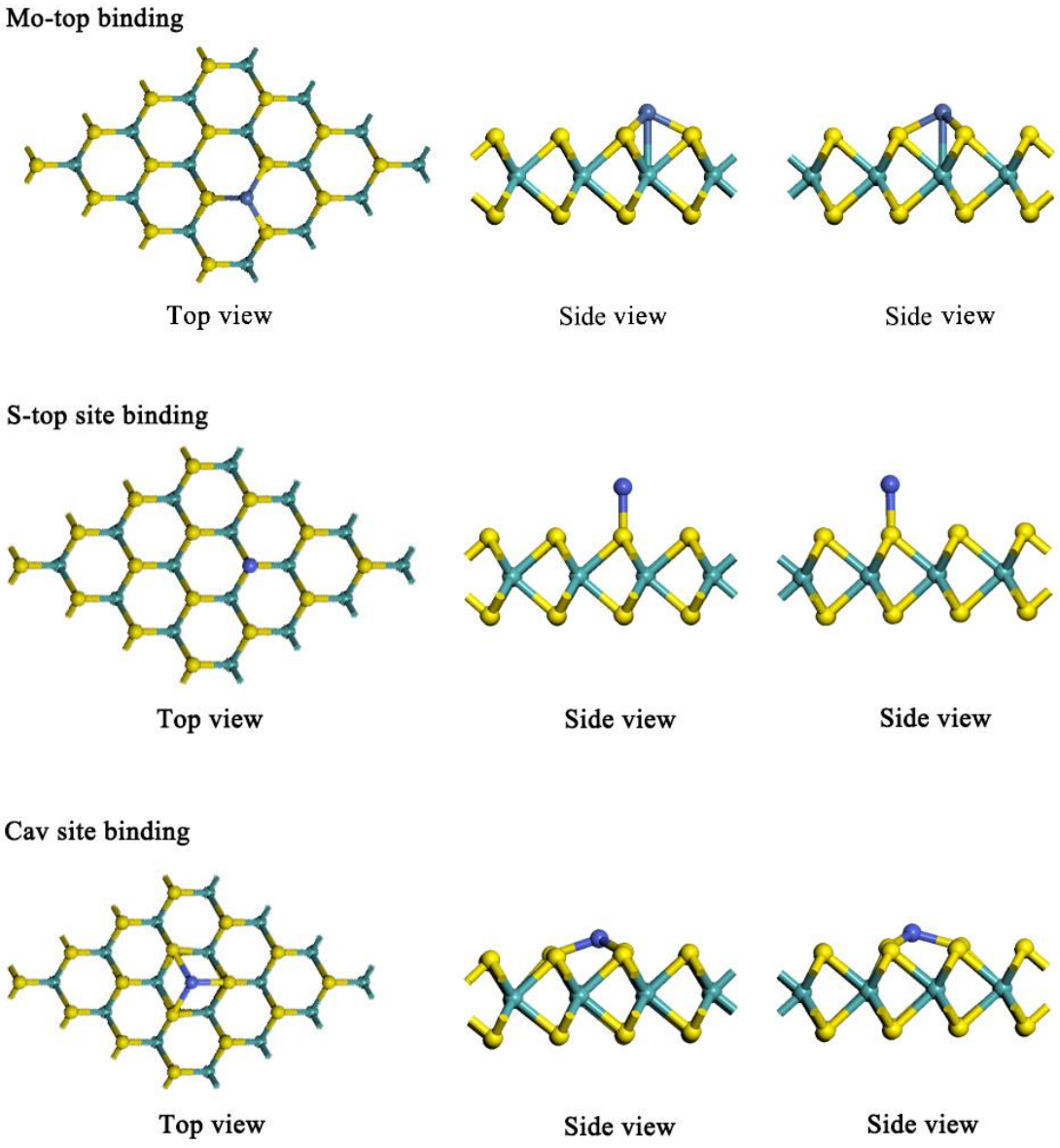

Figure S1. Illustration of three possible binding configurations (Related to Figure 1). Colour scheme for elements: yellow for S, cyan for Mo, blue for transition metal atoms.

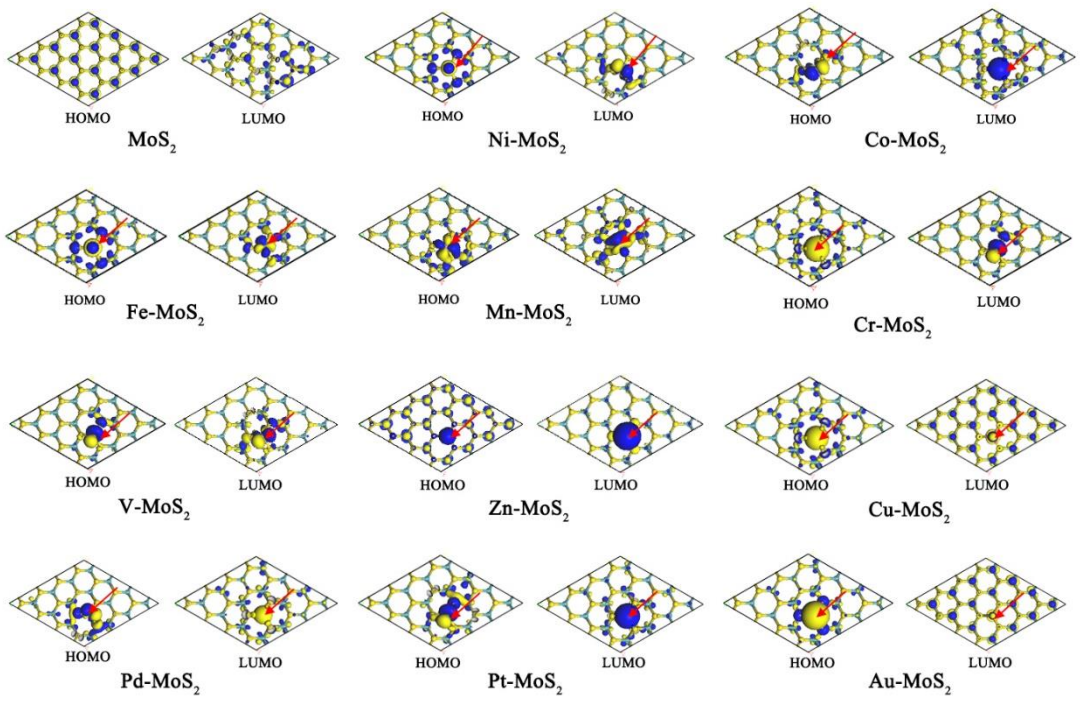

Figure S2. Spatial distribution of frontier orbitals (HOMO and LUMO) of different M-UMONs (Related to Figure 1). The red arrow indicates the surface transitional metal sites. These results showed the frontier orbital is intensively distributed at the surface metal sites, indiacting these sites are the main active sites (Chattaraj et al., 2003).

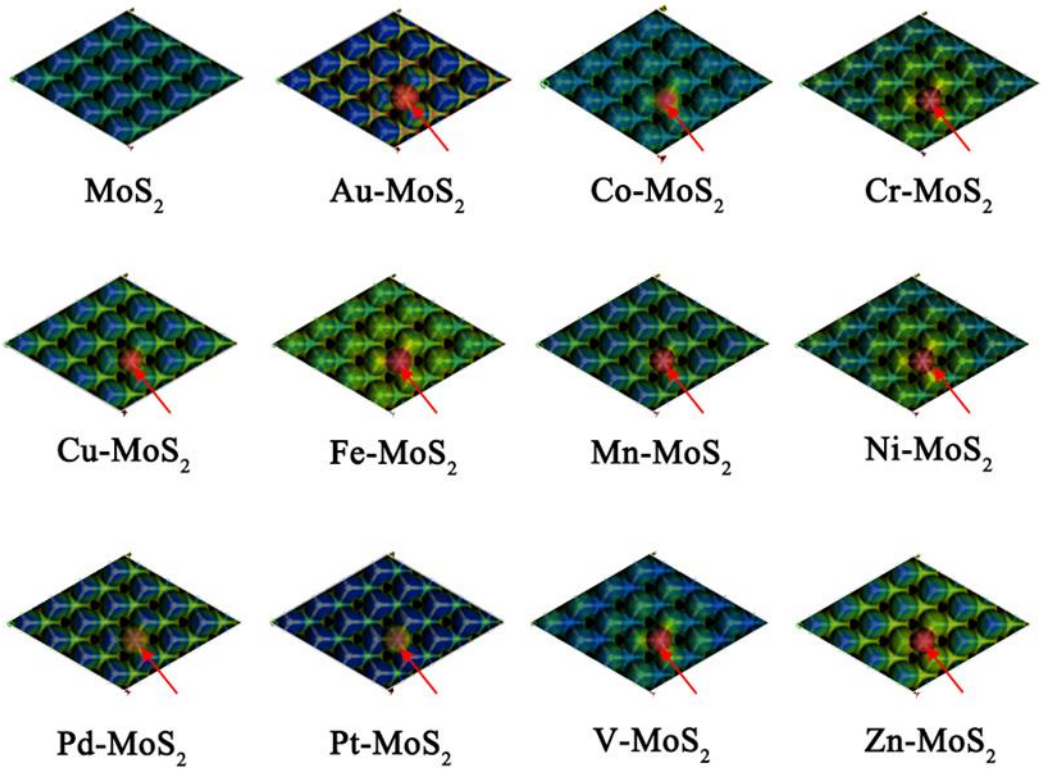

Figure S3. 3D electron density isovalue (isovalue = 0.2) surface mapped with ESP of different M-UMONs (the ESP value increases from blue to red) (Related to Figure 1). The red arrow indicates the surface transitional metal site. These results indicated the surface metal sites possess more positive ESP values, benefitting the adsorption of negative-charged OH^-.

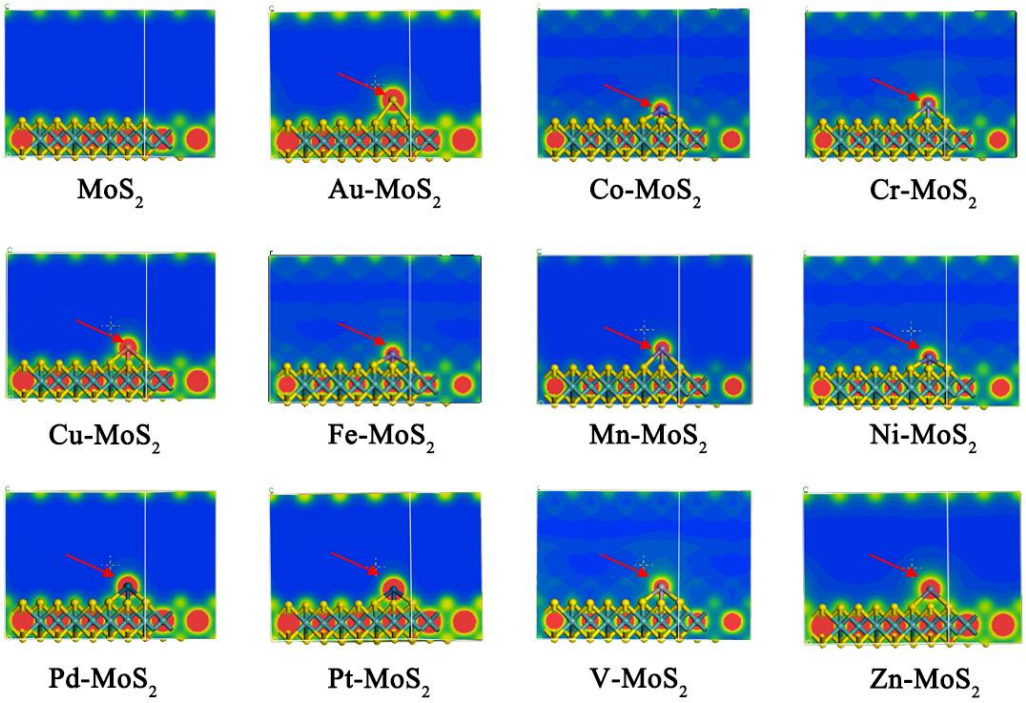

Figure S4. Sectional view of the ESP distribution (Related to Figure 1 and S3). The red arrow indicates the surface transitional metal site.

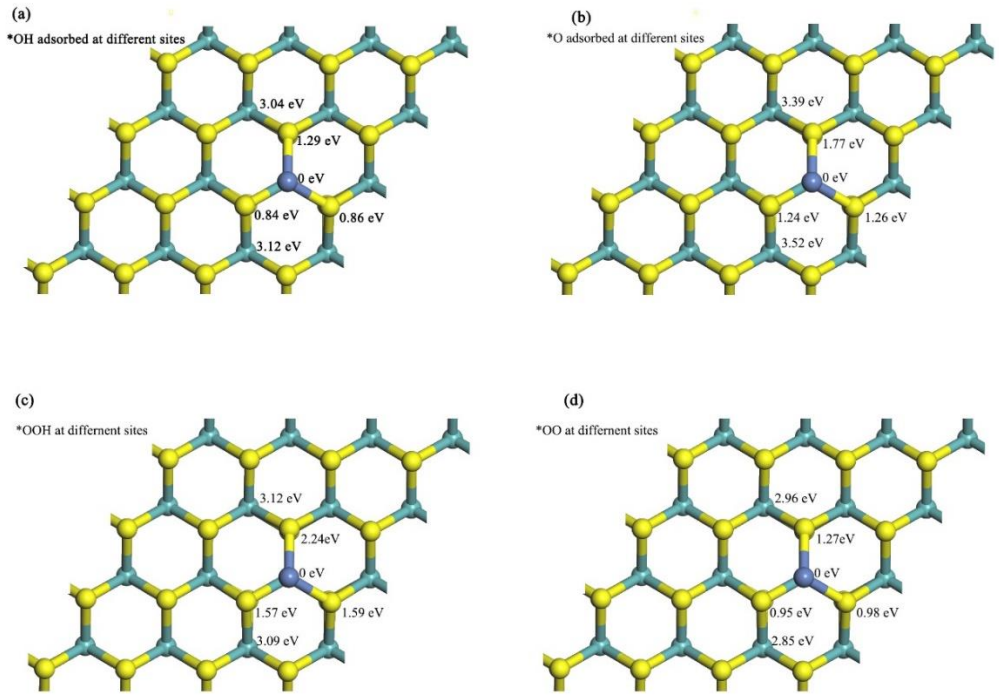

Figure S5. The adsorption energy of the OER intermediates at different surface sites of Ni-UMONs (Related to Figure 1). The value of surface Ni atom site is used as reference. The adsorption energy was calculated used below formula:

$$E_{ads} = E\,(A+B) - E\,(A) - E\,(B) + E(BSSE)$$

Here, the E_{ads} is the adsorption energy, E (A+B) is the total energy of intermediates and Ni-UMONs after adsorption. E (A) and E (B) are the total energy of the intermediates and Ni-UMONs, respectively (Mavrikakis et al., 1998). Specially, the E(BSSE) is the BSSE corrected energy and was calculated by the formula below:

$$E(BSSE) = [E(A) - E(A, bAB)] + [(E(B) - E(B, bAB)]$$

Here, E(A, bAB) is the energy of A with the basis set of both A and B, E(B, bAB) is the energy of B with the basis set of A and B. As shown above, the OER intermediates are energetically preferred to be adsorbed at surface metal sites. It should be noted that the basis set superposition error (BSSE) was taken into consideration since the adsorption energy was calculated and derived from the LCAO method.

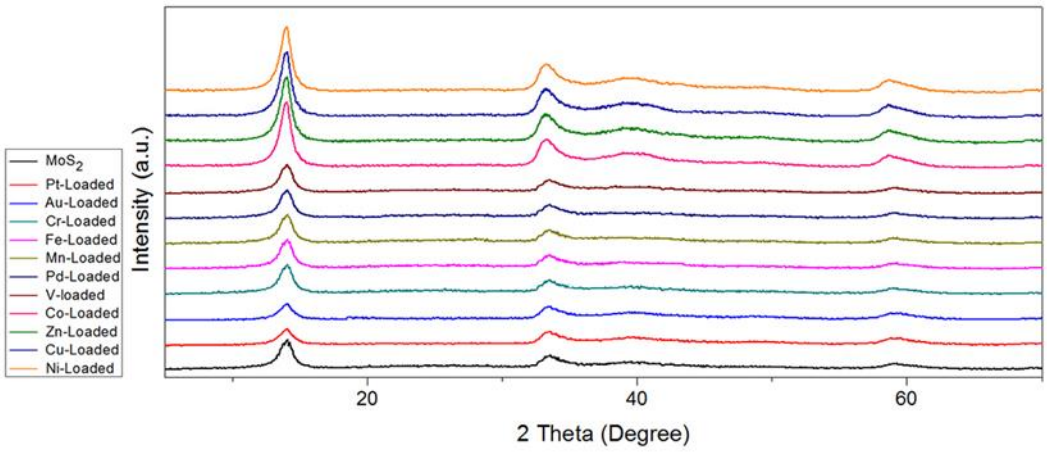

Figure S6. XRD patterns of MoS_2 nanosheets and different M-UMONs (Related to Figure 1). These results indicated that these M-UMONs share the same crystal structure with MoS_2 nanosheets, and no other peaks were detected, indicating the transition metal atoms were atomic dispersed on the surface of MoS_2. Besides, the strongest (002) diffraction peak in XRD patterns clarified plane (002) is the most exposed to the solution during OER process, proving that DFT calculations on plane (002) is rational.

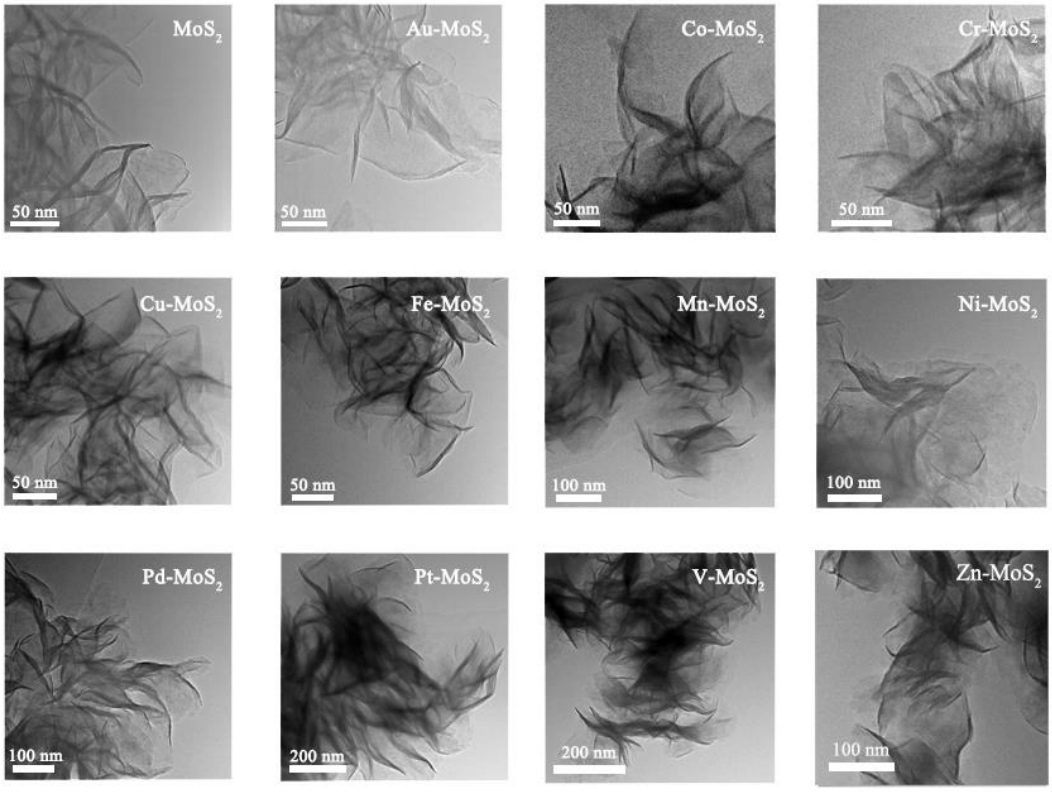

Figure S7. TEM images of different M-UMONs and MoS_2 nanosheets (Related to Figure 1). The TEM images indicate the M-UMONs have a 2D ultrathin morphology. Owing to the ultrathin flexible feature, the edges of the nanosheets curled spontaneously during drying (Zhao et al., 2016).

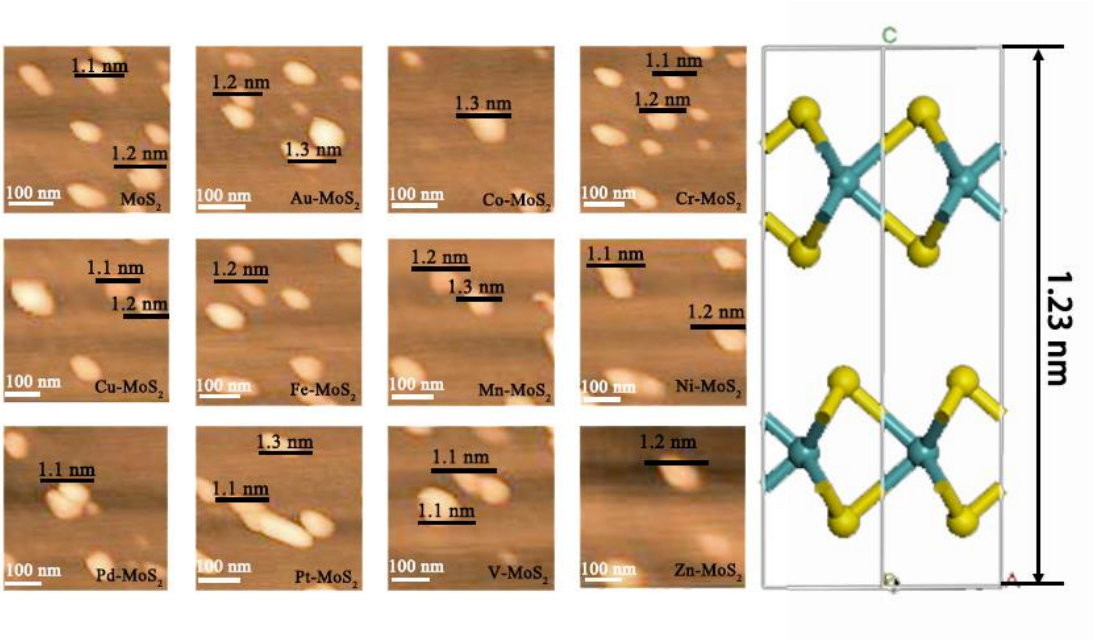

Figure S8. AFM images of different M-UMONs (Related to Figure 1). The right side shows theoretical thickness of MoS_2 nanosheet with two molecular layers. The AFM images indicates a uniform thickness of 1.2 nm, which corresponds to the two MoS_2 molecular layers.

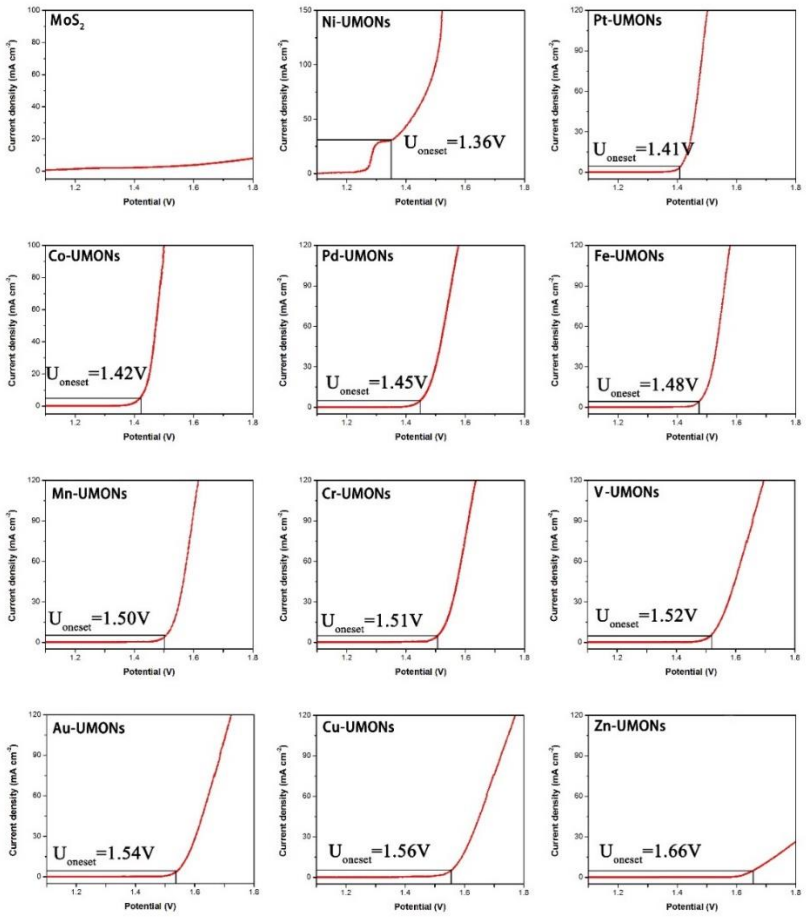

Figure S9. LSV curves of MoS_2 nanosheets and different kinds of M-UMONs (Related to Figure 4). The onset potential was defined as the potential at the current density of 5 mA cm^{-2}. The peak in 1.30 V ~ 1.35 V should be attributed to the oxidation of Ni (Zhao et al., 2016), and then the oneset potential of Ni-UMONs were roughly estimated at 1.36V. The redox potentials of other transition metal elements were not in this potential range, so no oxidation peak were observed during the electrochemical measurements. The negligible current of MoS_2 nanosheets confirmed that the surface transition metal atoms are the main active sites, that is to say, the active sites are usually at the edge of the 2D materials (Friebel et al., 2015). However, in this work, pure MoS_2 nanosheets could offer negligible OER activity, when the single metal atoms were supported on the surface of MoS_2 nanosheet, the significantly enhanced OER performance was observed. These results showed the OER activity was mainly from the supported single metal atoms rather than the edge defect sites, confirming our frontier orbitals calculation results. Besides, the experimental results matches well with the theoretical overpotentials, validating our high-throughput calculation results of theoretical overpotentials.

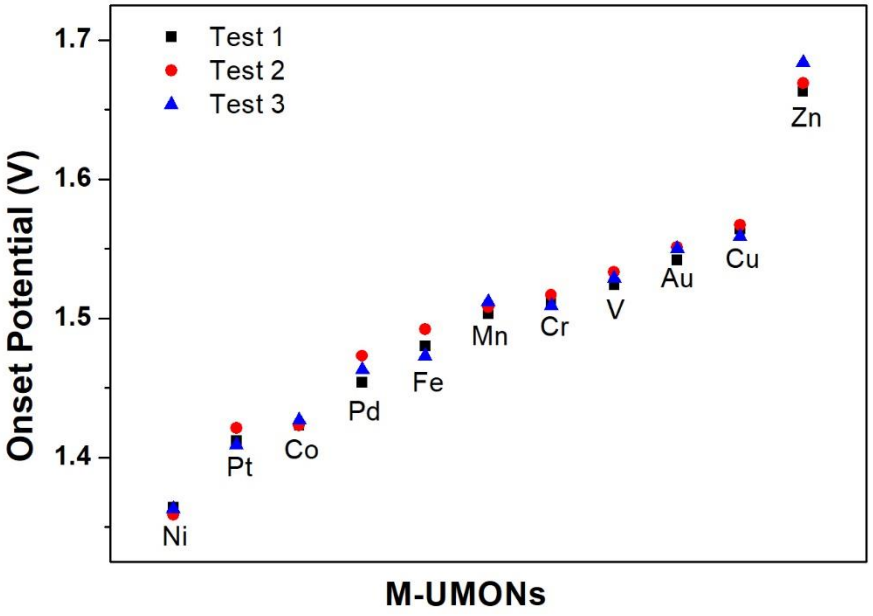

Figure S10. The onset potential of different kinds of M-UMONs in three parallel tests (Related to Figure 4). These results indicate that our experimental results were credible, and no obvious differences were observed between these parallel tests.

Figure S11. M-S bond orders of different kinds of M-UMONs (Related to Figure 2, 3 and 4). The M-S bond orders values are displayed below the associated element symbol.

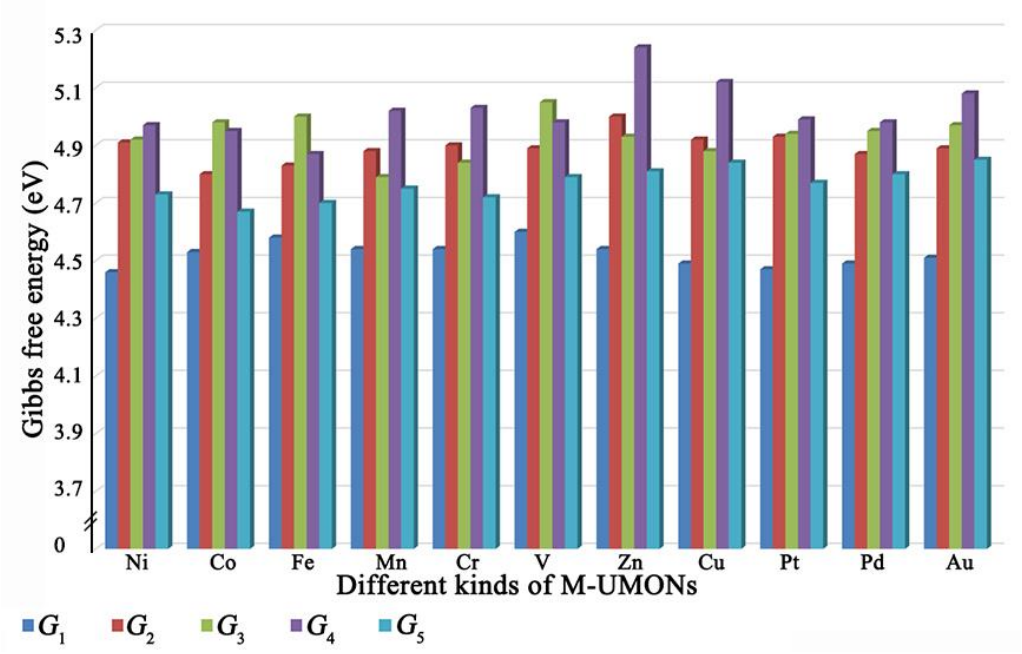

Figure S12 Gibbs free energy diagram of the OER process of above mentioned eleven kinds of M-UMONs (Related to Figure 4).

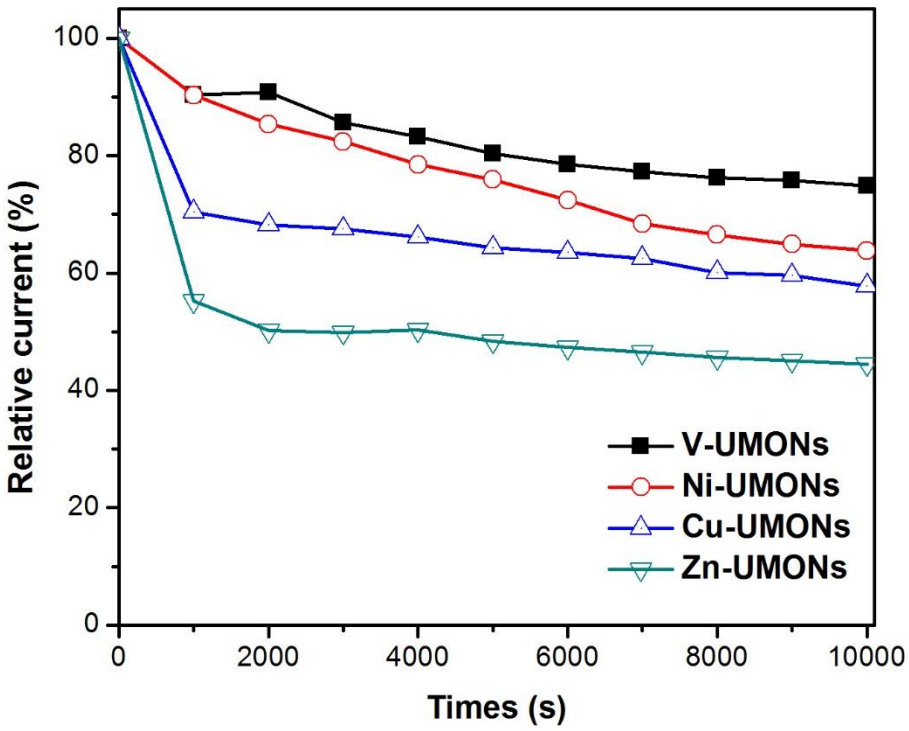

Figure S13. Chronoamperometric curves of V-UMONs, Ni-UMONs, Cu-UMONs and Zn-UMONs at the overpotential of 0.4 V (Related to Figure 3 and 4). These results indicated the tendency of catalysts stability is consistent with that of the M-S bond orders, which confirms our bond population calculations is rational.

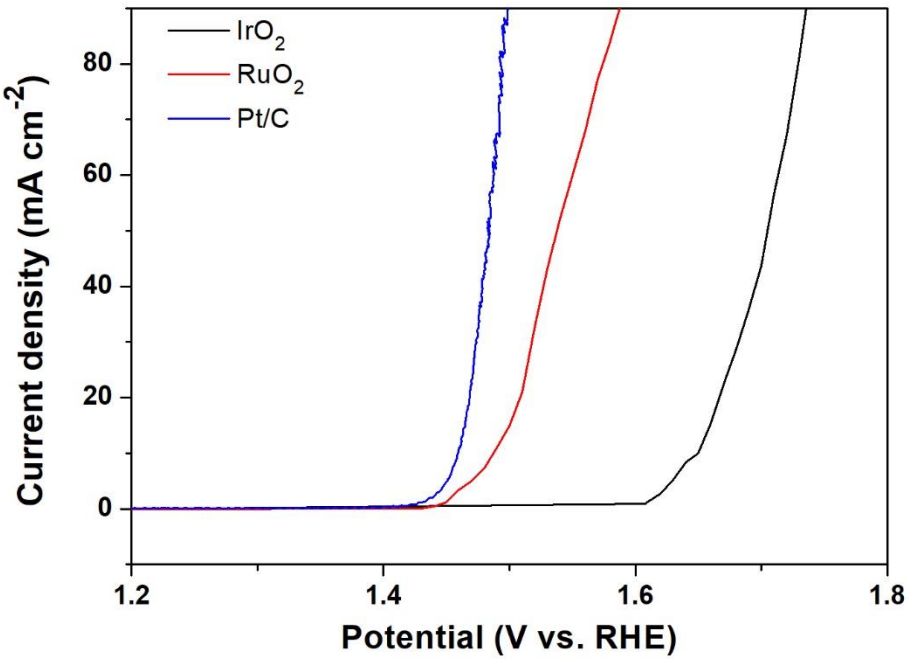

Figure S14. The LSV curves of commonly used OER catalysts including IrO_2, RuO_2 and Pt/C (Related to Figure 4 and S9). These results indicate that Ni-UMONs, Co-UMONs and Pt-UMONs could offer comparable performance and even outperform these commonly used OER catalysts. These results also confirmed construction of M-UMONs is a practical pathway to develop high-performance OER catalysts.

Supplemental Tables

Items	Mo-top site[a]	S-top site	Cav-site
Ni-MoS_2	0	1.25	0.42
Co-MoS_2	0	1.55	0.46
Fe-MoS_2	0	0.94	0.24
Mn-MoS_2	0	0.38	0.24
Cr-MoS_2	0	0.41	0.14
V-MoS_2	0	0.86	0.44
Zn-MoS_2	0	0.39	0.02
Cu-MoS_2	0	0.36	0.07
Pd-MoS_2	0	0.14	0.14
Pt-MoS_2	0	0.06	0.33
Au-MoS_2	0	0.27	0.04

Table S1. Relative energy (eV) of different transition metal atoms binding configurations (Related to Figure 1).

[a]The energy of Mo-top configuration is used as reference.

Items	Transition metal	Mo	S	M(at%)
Ni-MoS_2	1.57	58.21	40.22	4.29
Co-MoS_2	1.63	59.32	39.05	4.43
Fe-MoS_2	1.51	59.18	39.31	4.33
Mn-MoS_2	1.47	59.56	38.97	4.28
Cr-MoS_2	1.37	60.27	38.36	4.22
V-MoS_2	1.42	59.42	39.16	4.46
Zn-MoS_2	1.31	59.27	39.42	3.21
Cu-MoS_2	1.54	59.09	39.37	3.88
Pd-MoS_2	1.53	59.71	38.76	2.30
Pt-MoS_2	1.82	60.03	38.15	1.49
Au-MoS_2	1.48	59.20	39.32	1.20

Table S2. ICP-MS results (wt %) and derived atomic percentage (at%) of transition metal atoms of different kinds of M-UMONs (Related to Figure 1).

M-UMONs	Basis set	Mayer Bond Orders
Ni-S	DNP	0.8428/0.8712/0.8501
	DND	0.8419/0.8709/0.8505
Co-S	DNP	0.8696/0.9351/0.8679
	DND	0.8699/0.9350/0.8676
Fe-S	DNP	0.8847/0.9938/0.8859
	DND	0.8841/0.9935/0.8853
Mn-S	DNP	0.7724/0.8193/0.7691
	DND	0.7723/0.8190/0.7689
Cr-S	DNP	0.7582/0.7794/0.7577
	DND	0.7584/0.7791/0.7576

Table S3. The calculated Mayer bond orders with different basis set (Related to Figure 2 and 3). This result showed that Mayer bond order is almost keep unchanged when the basis set changed.

Supplemental References

Mayer, I. (1986). Bond orders and valences from ab initio wave functions. Int. J. Quantum Chem. *29*, 477-483.

Torres, J. A., Santiago, L. R., Sodupe, M. and Rauk, A. (2011). Structures and stabilities of $Fe^{2+/3+}$ complexes relevant to alzheimer's disease: an ab initio study. J. Phys. Chem. A *115*, 12523-12530.

Liu, G., Robertson, A. W., Li, M. M.-J., Kuo, W. C. H., Darby, M. T., Muhieddine, M. H., Lin, Y.-C., Suenaga, K., Stamatakis, M., Warner, J. H., and Tsang, S. C. E. (2017). MoS2 monolayer catalyst doped with isolated Co atoms for the hydrodeoxygenation reaction. Nat. chem. 9, 810-816.

Stevens, M. B., Enman, L. J., Batchellor, A. S., Cosby, M. R., Vise, A. E., Trang, C. D. M., and Boettcher, S. W. (2017). Measurement techniques for the study of thin film heterogeneous water oxidation electrocatalysts. Chem. Mater. *29*, 120-140.

Zhuang, Z., Sheng, W., and Yan, Y. (2014). Synthesis of monodispere Au@Co_3O_4 core-shell nanocrystals and their enhanced catalytic activity for oxygen evolution reaction. Adv. Mater. *26*, 3950-3955.

Chattaraj, P. K., Maiti, B., and Sarkar, U. (2003). Philicity: a unified treatment of chemical reactivity and selectivity. J. Phys. Chem. A *107*, 4973-4975.

Mavrikakis, M., Hammer, B., and Nørskov, J. K. (1998). Phys. Rev. Lett. *81*, 2819-2822.

Zhao, S., Wang, Y., Dong, J., He, C.-T., Yin, H., An, P., Zhao, K., Zhang, X., Gao, C., Zhang, L., Lv, J., Wang, J., Zhang, J., Khattak, A. M., Khan, N. A., Wei, Z., Zhang, J., Liu, S., Zhao, H., and Tang, Z. (2016). Ultrathin metal–organic framework nanosheets for electrocatalytic oxygen evolution. Nat. Energy *1*, 16184.

Zhao, S., Wang, Y., Dong, J., He, C.-T., Yin, H., An, P., Zhao, K., Zhang, X., Gao, C., Zhang, L., Lv, J., Wang, J., Zhang, J., Khattak, A. M., Khan, N. A., Wei, Z., Zhang, J., Liu, S., Zhao, H., and Tang, Z. (2016). Ultrathin metal–organic framework nanosheets for electrocatalytic oxygen evolution. Nat. Energy *1*, 16184.

Friebel, D., Louie, M. W., Bajdich, M., Sanwald, K. E., Cai, Y., Wise, A. M., Cheng, M.-J., Sokaras, D., Weng, T.-C., Alonso-Mori, R., Davis, R. C., Bargar, J. R., Nørskov, J. K., Nilsson, A., Bell, A. T. (2015). Identification of Highly Active Fe Sites in (Ni,Fe)OOH for Electrocatalytic Water Splitting. J. Am. Chem. Soc. *137*, 1305-1313.